

## The Flat Fielding and Achievable Signal-to-Noise of the MAMA Detectors<sup>1</sup>

Mary Elizabeth Kaiser<sup>2</sup>

*The Johns Hopkins University, Department of Physics and Astronomy, Baltimore, MD 21218*

Don J. Lindler

*Advanced Computer Concepts, Inc, Potomac, MD 20805*

Ralph C. Bohlin

*Space Telescope Science Institute, 3700 San Martin Drive, Baltimore, MD 21218*

**Abstract.** The Space Telescope Imaging Spectrograph (STIS) was designed to achieve a signal-to-noise of at least 100:1 per resolution element. MAMA observations during Servicing Mission Orbital Verification (SMOV) confirm that this specification can be met. From analysis of a single spectrum of GD153, with counting statistics of  $\sim 165$  a S/N of  $\sim 125$  is achieved per spectral resolution element in the FUV over the spectral range of 1280Å to 1455Å. Co-adding spectra of GRW+70D5824 to increase the counting statistics to  $\sim 300$  yields a S/N of  $\sim 190$  per spectral resolution element over the region extending from 1347Å to 1480Å in the FUV. In the NUV, a single spectrum of GRW+70D5824 with counting statistics of  $\sim 200$  yields a S/N of  $\sim 150$  per spectral resolution element over the spectral region extending from 2167 to 2520Å. Details of the flat field construction, the spectral extraction, and the definition of a spectral resolution element will be described in the text.

### 1. Introduction

The first generation HST instruments spent considerable effort to devise flat field calibrations for their detectors in the UV. As areal detectors, this was a problem for FOC and WFPC in particular. Time was spent generating streak flats by observing the bright earth limb, but despite heroic efforts the method did not work well and the S/N suffered. Having witnessed the efforts expended to obtain in-flight flat fields, UV flat field calibration lamps were installed in STIS. Acquiring both the pre- and post-launch data and the subsequent derivation of a flat for each of the MAMA detectors has been a very iterative and time consumptive process. The end results of these endeavors are contained in section 4 on signal-to-noise.

In the ultraviolet, STIS employs a less familiar detector technology to achieve relatively high throughput over this bandpass. For this reason and the difficulty in obtaining large-area UV flat fields, the achievable signal-to-noise has been a key issue for the UV bands.

---

<sup>1</sup>Based on Observations with the NASA/ESA *Hubble Space Telescope*, obtained at the Space Telescope Science Institute, which is operated by the Association of Universities for Research in Astronomy, Inc. (AURA), under NASA contract NAS5-26555.

<sup>2</sup>Co-Investigator, STIS Investigation Definition Team

In the FUV (1150-1700Å), STIS employs a  $1024 \times 1024$  Multi-anode Microchannel Array (MAMA) with an inclined, planar window and a CsI photocathode deposited directly on the microchannel plate (MCP). The NUV (1650-3100Å) MAMA has a CsTe photocathode deposited directly on the inside of its non-inclined window. Due to the tilt of the window on the front of the FUV MAMA, the flat fields for this bandpass are more susceptible to variations as a function of angle of incidence. Consequently, the FUV flat fields may be optical mode dependent.

Both detectors are read-out in high-res mode, whereby the processing electronics centroid event positions to half the spacing of the  $1024 \times 1024$  element anode array. This high-resolution readout mode provides higher resolution, but unfortunately flat field variations are much larger, exhibiting a pronounced ( $\sim 45$ - $50\%$ ) odd-even amplitude variation. Except where noted, the results in this paper will refer to the low-resolution pixels in the  $1024 \times 1024$  format (Kimble et al. 1998).

Intrinsic pixel-to-pixel variations are 3.9% and 2.8% rms for the FUV and NUV MAMA, respectively, in the  $1024 \times 1024$  low-res pixel format. Ground flat fields for both flight MAMA detectors have shown excellent long term stability, particularly in the low-res mode:  $<1.0\%$  rms variations over time scales of weeks to months. The pixel-to-pixel flat-field variations of the NUV MAMA show little dependence on wavelength or angle of incidence. Consequently, flat fields have been constructed at a  $S/N > 300$  per resolution element ( $2 \times 2$  low-res pixels) that can be applied to all NUV modes (Bohlin, Lindler, and Kaiser 1997).

In the FUV, there is also little dependence on wavelength. However, due to the inclined window on the FUV MAMA detector, the angle of incidence effects are not as negligible as in the NUV. As a consequence of the mode dependence of the flats detected during the ground-based calibration program, FUV flat fields were taken in the echelle modes as well as the first order spectroscopic modes.

Construction of the FUV and NUV flats are similar in principle but differ in practice. The NUV flat field has been installed in both the IDT and STScI calibration pipelines, whereas the FUV flat is still undergoing test and refinement. Pipeline delivery is expected in the near future.

In section 2, we describe the acquisition of flat-field calibration data in ground-testing. Section 3 presents the detailed methodology for construction of the final flats. Section 4, of greatest interest to the general observer, presents the  $S/N$  achieved in actual in-flight observations with and without applying the ground-based flats.

## 2. Ground Flat Field Calibrations

Contemporaneous analysis of the NUV flat fields during ground-based calibration verified that the flat field construction method outlined in Bohlin, Lindler, and Baum 1996 (hereafter BLB) was valid. Mode G230M exposures of the internal deuterium calibration lamp were acquired in addition to exposures with an external deuterium continuum lamp.

Internal lamp use was limited to a sufficient number of exposures to confirm the flat field stability and to acquire a pixel-to-pixel detector flat (requiring a  $S/N$  of 100:1 per pixel) as a baseline comparison for in-flight pixel-pixel flats. The NUV flat field currently in the pipeline consists solely of this ground based data set.

It should be noted that acquisition of flat fields with large format, count-rate limited detectors requires a significant investment of time. Acquiring a pixel-pixel flat, composed of 13 consecutive exposures, to yield a total  $S/N$  of 100:1 per pixel at a single grating position ( $\lambda 2659$ ) consumed 13 hours. This is a best case result: a mode with uniform illumination of the detector, a count-rate well-matched to the limits imposed during ground calibrations ( $300,000$  counts  $s^{-1}$ ), and with minimal exposure overheads.

Due to the detection of angle of incidence effects in the FUV flats during the latter period of the ground calibration, the strategy for acquiring FUV flats was modified. A

campaign of acquiring flats at the required S/N of 100:1 per resolution element for each mode with the external UV lamps was initiated. Since the Kr lamp continuum spans a limited spectral range (1280-1700Å), where the flux beyond 1500Å is dropping rapidly, additional exposures were required using an external argon lamp at the short end of the bandpass and an external xenon lamp at the longest wavelengths.

Furthermore, illumination of the nominal inter-order format on the echelle detectors required additional exposures with the cross-dispersion grating tipped slightly from the nominal position to illuminate the inter-order pixels. The FUV flat field exposures used to construct the FUV super-flat are the set of E140M and E230M ground-based data taken with the external argon, krypton, and xenon lamps, in addition to the in-flight G140L and G140M ( $\lambda 1272$  and  $\lambda 1518$ ) data.

### 3. Flat Field Construction

Algorithms have been defined (BLB) for deriving the STIS MAMA flats. We employ the terminology defined in that document here. The overall strategy is to separate the illuminating lamp signature from the high frequency structure of the MAMA flat itself. However, one major modification to the initial formalism was required due to the presence of irregularities ( $>1\%$ ) in the slit widths for the long slits. The introduction of a correction  $W$  for slit width variations can correct all but the largest defects in the NUV to 1% precision.  $W$  is an average over wavelength and is a function of pixel position along the slit. The 1-D function  $W$  is the raw flat data image collapsed along the spectral direction and is analogous to the orthogonal correction,  $R_L(\lambda)$ , which is the average lamp spectrum collapsed along the slit direction and is used to correct the flat field images for narrow emission lines.

In addition to the illumination variation resulting from the lamp spectral and spatial response and the slit non-uniformity, there is also a contribution due to the HST Optical Telescope Assembly(OTA)+STIS vignetting. This low frequency correction awaits analysis of post-launch calibration data. In practice the flats are constructed by geometrically correcting the original co-added image to make the dispersion and spatial axes parallel to the  $x$  and  $y$  axes of the rotated image. Then the corrected image is collapsed along the separate axes to obtain the spectral S-flat and the W-flat averages. Following this, the inverse geometric distortion correction is applied to transform the WS-flat product image back to the original distorted space. The original image,  $R_L$  is then divided by the transformed WS-flat template. Fiducials, the long-slit occulting bars near the detector edge in the nominal position, are filled in the non-dithered flats and other problem regions are then masked. Filtering is then applied to the flat to obtain the overall 2-D illumination function (L-flat) for that mode. Division of the flat by the L-flat yields the pixel-pixel detector response (P-flat). Thus the P-flat is simply obtained by removing the lamp signature from the original co-added  $R_L$  image and then dividing by the L-flat as rebinned to the original  $2048 \times 2048$  high-res size. The L-flat and the P-flat are both normalized to unity in the central region.

#### 3.1. NUV Flat Fields

Table 1 compares each of the first 11 P-flats to the extreme wavelength 2977Å flat with the best statistics. The entries are the one sigma values for ratios of images. Image ratios test the similarity of the flat fields at different wavelengths. The first row for each of the three image sizes is the expected sigma from counting statistics, the second row is the actual scatter in the ratio images, and the third row measures the actual difference between the two ratioed images. In other words, these third rows of each set are the actual scatter with the Poisson uncertainty removed in quadrature. The results are consistent with no wavelength dependence and little MAMA contribution to the scatter per low-res pixel or per resolution element. There is a residual scatter of a few percent in the high-res ratios,

which demonstrates the nearly complete removal of the large 60% pixel-to-pixel scatter of the high-res flats. Since the tabulated Poisson statistics utilize the average counts, the Poisson entries for the high-res case are underestimates of sigma because of the large change in sensitivity between adjacent pixels due to the odd-even effect in the MAMA electronics. The corresponding high-res residuals are overestimates.

Table 1. Statistics for the Ratio of NUV Flat Fields to the 2977Å Flat

	1769	1933	2176	2419	2419	2419	2659	2659	2659	2659	2977
P FLATS (512x512)											
Poisson (%)	1.23	1.38	1.33	2.05	1.50	1.99	1.05	1.65	2.09	1.25	2.07
Actual sigma (%)	1.24	1.41	1.33	2.04	1.50	2.02	1.07	1.64	2.07	1.33	2.06
Resid. sigma (%)	0.20	0.27	0.00	0.00	0.02	0.38	0.19	0.00	0.00	0.46	0.00
P FLATS (1024x1024)											
Poisson (%)	2.45	2.77	2.67	4.09	2.99	3.98	2.10	3.29	4.18	2.50	4.14
Actual sigma (%)	2.47	2.80	2.67	4.02	2.99	4.01	2.12	3.31	4.17	2.63	4.13
Resid. sigma (%)	0.29	0.42	0.12	0.00	0.11	0.56	0.34	0.31	0.00	0.80	0.00
P FLATS (2048x2048)											
Poisson (%)	4.91	5.53	5.33	8.18	5.98	7.95	4.19	6.59	8.35	5.00	8.28
Actual sigma (%)	5.72	6.47	6.15	8.96	6.89	12.18	4.87	7.25	9.63	11.01	9.55
Resid. sigma (%)	2.95	3.34	3.05	3.66	3.42	9.22	2.48	3.04	4.79	9.81	4.75

Ground-based NUV flats were obtained during two time intervals. The first data set was obtained during August and September 1996 while in thermal vacuum at Ball Aerospace. After shipping the instrument to GSFC, a second set of flats was acquired under nitrogen purge during November 1996. The two sets of flats exhibit residual structure as illustrated most strongly in the high-res residual of 9.81% in the last row of Table 1. The other P-flat data obtained in November 1996 is at 2419A and also has a high residual of 9.22% per high-res pixel at image center.

Since the 1769 and 1933A flats have illumination along only the central third of the slit, the superflat is the combination of the Ball data at the G230M central wavelengths of 2176, 2419, 2659, and 2977A and is shown in Figure 1. The Poisson statistic of 0.30% per resolution element for the superflat correspond to a S/N=333 in regions without fiducial or slit defect masks. On-orbit flats are required to quantify changes, which degrade S/N achieved when this superflat is applied to flight data.

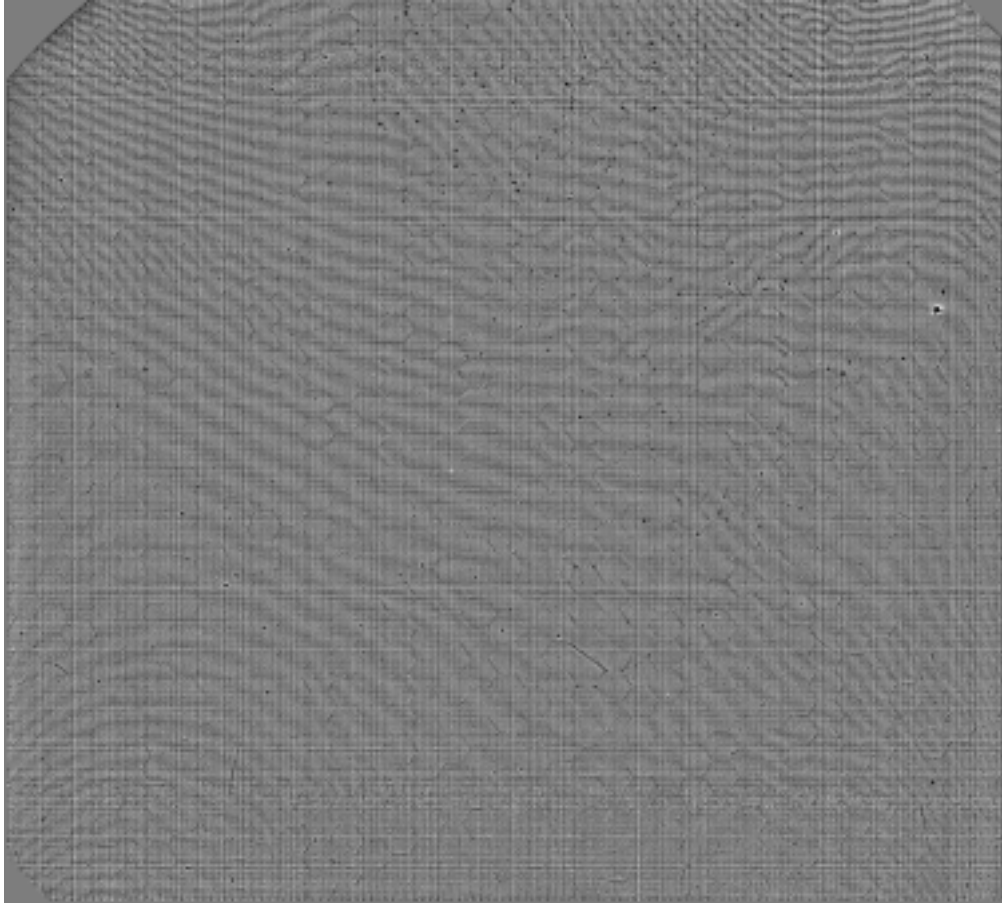
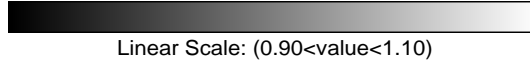


Figure 1: Combined NUV Flat Field

### 3.2. FUV Flat Fields

The formalism applied for the FUV mirrors the NUV procedure. However, all the images except the G140M ( $\lambda 1518$ ) exposure had limited spectral coverage which required masking large regions of unilluminated regions on the flat. In addition, the echelle images with the argon and xenon lamps were taken with the  $0.5'' \times 0.5''$  arcsec slit, thus broadening emission lines from these lamps which required masking prior to removal of the illumination signature from the data. From the set of echelle images, a flat has been created which is illuminated over nearly the full field. A few unilluminated regions of limited extent remain. These are the result of inter-order rows which remain unilluminated despite the slight offset of the cross-disperser grating position, or the repeller wire (an electrode above the MCP which prevents photoelectrons created by the MCP from escaping) shadow in the echelle modes which requires masking but this region of the detector will be fully illuminated with a more complete set of first order flats. A few isolated emission line regions persist, but will also be illuminated by either a more complete set of first order flats or echelle flats with the internal krypton lamp.

The addition of the post-launch G140L and G140M flat field images also provides nearly complete illumination of the detector. However, a  $52'' \times 0.05''$  ND filtered slit was used to acquire the G140M data set. Residuals from filtering this slit's prominent features

were masked. Pending command development, the slit wheel was used solely at the nominal setting thus leaving regions shadowed by the fiducials unilluminated.

In the spectral direction, the G140L and G140M( $\lambda 1272$ ) images are unilluminated for wavelengths below  $\sim 1280\text{\AA}$ . Thus the G140M( $\lambda 1272$ ) image provides illumination of the longest wavelength pixels in the G140L image where the flux is rapidly decreasing. The G140M( $\lambda 1518$ ) image provides illumination at pixels corresponding to the shortest wavelengths in the G140L image.

Combination of the G140L and G140M data sets provides nearly complete illumination of the detector at a S/N, derived purely from counting statistics, of 150 per  $2 \times 2$  pixel resolution element at the longest wavelengths where the counting statistics are poorest. Masked fiducial shadows in the G140M flats can be filled by the proposed commanding to move the slit from its nominal position in the spatial direction when acquiring flats with the fiducial slits.

In constructing the echelle flats, for the addition of each set of images at a unique central wavelength, the ratio of the new composite flat to a single flat was calculated. In all instances, the image ratio errors decreased as the data were combined. The image ratio test was then executed for flats in different modes; the results are presented in Tables 2 and 3. Table 2 presents the results for a single flat field image in mode G140L relative the remaining G140L images. The subset of G140L flats are then combined with flats in the remaining modes. Table 3 presents the image ratio results for the combined G140L flat relative to the other modes.

Table 2. Statistics for the Ratio of a single FUV G140L 1425 $\text{\AA}$  Flat Field to the Composite Flats

	G140L	(G140L + G140M)	(G140L + G140M + E140M)	(G140L + G140M + E140M + E140H)
P FLATS (1024x1024)				
Poisson (%)	2.30	2.53	2.17	1.94
Actual sigma (%)	2.70	3.02	2.85	2.76
Resid. sigma (%)	1.40	1.65	1.84	1.96
P FLATS (2048x2048)				
Poisson (%)	5.05	5.58	5.14	4.87
Actual sigma (%)	5.64	5.98	8.18	9.02
Resid. sigma (%)	2.50	2.15	6.37	7.59

Table 3. Statistics for the Ratio of the FUV G140L Flat Field to the Flats from Other Modes

	G140M	E140M	E140H
P FLATS (1024x1024)			
Poisson (%)	3.23	2.20	1.49
Actual sigma (%)	4.02	3.16	2.47
Resid. sigma (%)	2.39	2.27	1.96
P FLATS (2048x2048)			
Poisson (%)	7.14	5.16	3.63
Actual sigma (%)	11.23	11.65	9.07
Resid. sigma (%)	8.67	10.45	8.31

From a visual inspection of the flat ratios it is apparent that there is  $\leq 5\%$  residual effect in removing an overall fringe pattern in the FUV flats. This fringe pattern can

be seen in both the NUV (Figure 1) and FUV flats (Figure 2). Despite this residual, a flat field composite of all the prime FUV observing modes (G140L, G140M, E140M and E140H) can be constructed and used to improve the achievable S/N for a given spectrum. The improvements attainable will be described further in the S/N section. Further in-orbit flats are required to monitor the FUV flat field stability and to improve the counting statistics in poorly illuminated regions (i.e. under fiducials, masked emission line regions). In addition, the use of one mode to correct another mode limits the achievable S/N. More data is required to isolate the dependence of this effect on post versus pre launch data versus mode dependence.

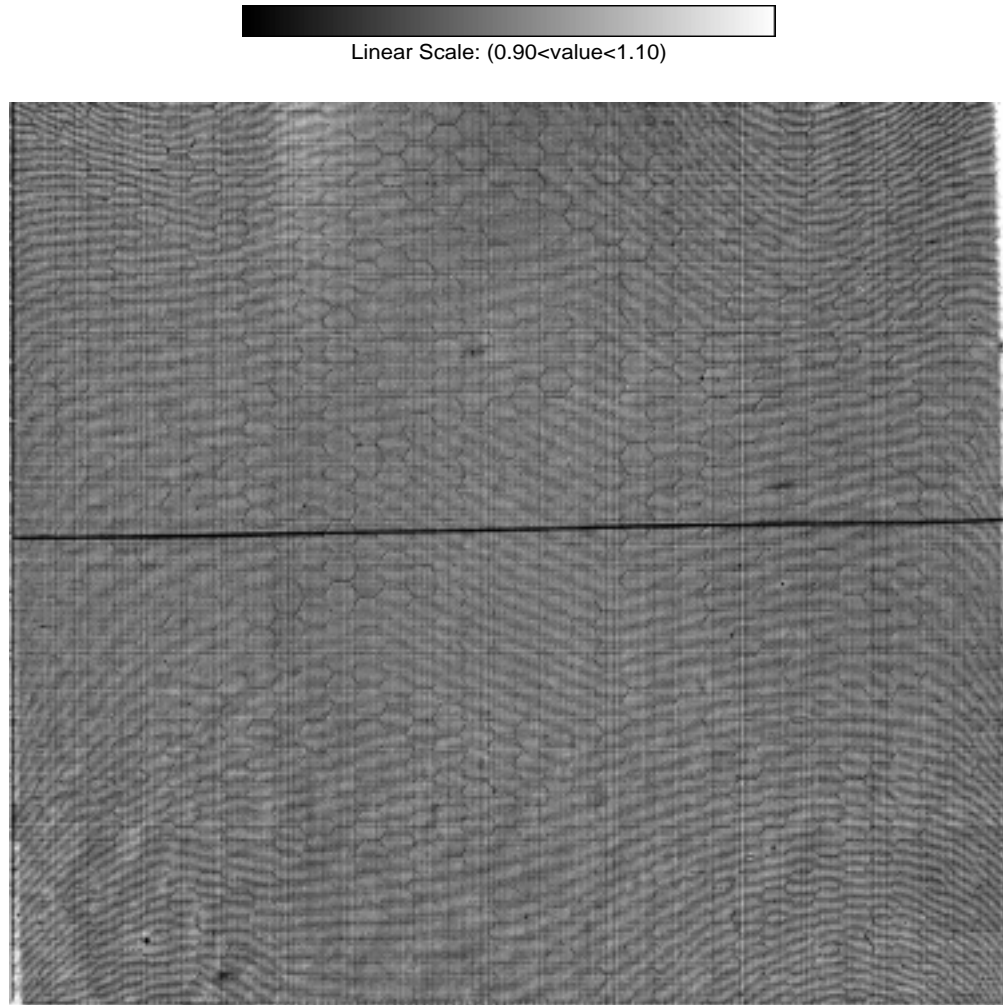


Figure 2: Combined FUV Flat Field

#### 4. Signal-to-Noise

Spectra of GD153 in mode G140L and GRW+70D58 in mode G140M were flat fielded to determine the realizable S/N. In practice, the IDT calibration pipeline employs a spectral extraction height of 11 pixels (spatial direction) and the spectral resolution is nominally two pixels. Therefore the S/N quoted for a point source in the first order modes, as defined in this paper, is per spectral resolution element ( $11 \times 2$  pixels).

Initially the data is background subtracted, then extracted, and binned in the spectral direction. The 1-D spectrum is then partitioned into segments composed of 20 bins each

which are fit with a cubic spline. Each segment is divided by its fit; the mean and standard deviation are calculated and ratioed to determine the S/N for each segment. The average of the S/N over the spectral segments contained within the specified spectral range is tabulated in Table 4 for the NUV and Table 5 for the FUV. For the NUV MAMA, the GRW+70D58 spectrum has a peak potential S/N, corresponding to pure counting statistics, of  $\sim 200$  per spectral resolution element. The realized S/N is  $\sim 105$  *without the application of a flat field* and  $\sim 150$  after application of the NUV flat field. For the FUV MAMA, the GD153 spectrum has a peak potential S/N, corresponding to pure counting statistics, of  $\sim 165$  per spectral resolution element. The realized S/N is  $\sim 85$  *without the application of a flat field* and  $\sim 130$  after application of the FUV flat field.

Table 4. NUV Signal-to-Noise Capabilities for a G230L Point Source Spectrum

Star	Spectral Class (B Mag)	Exposure Time	Flat Composition	Spectral Range	S/N (Counting Statistics)	S/N
GRW+70D58	DA3 (12.63)	636.0	NO Flat	1698 - 2167	<165>	<100>
				2167 - 2520	<204>	<101>
				2520 - 3050	<163>	<102>
			G230M	1698 - 2167	<165>	<154>
				2167 - 2520	<204>	<149>
				2520 - 3050	<163>	<152>

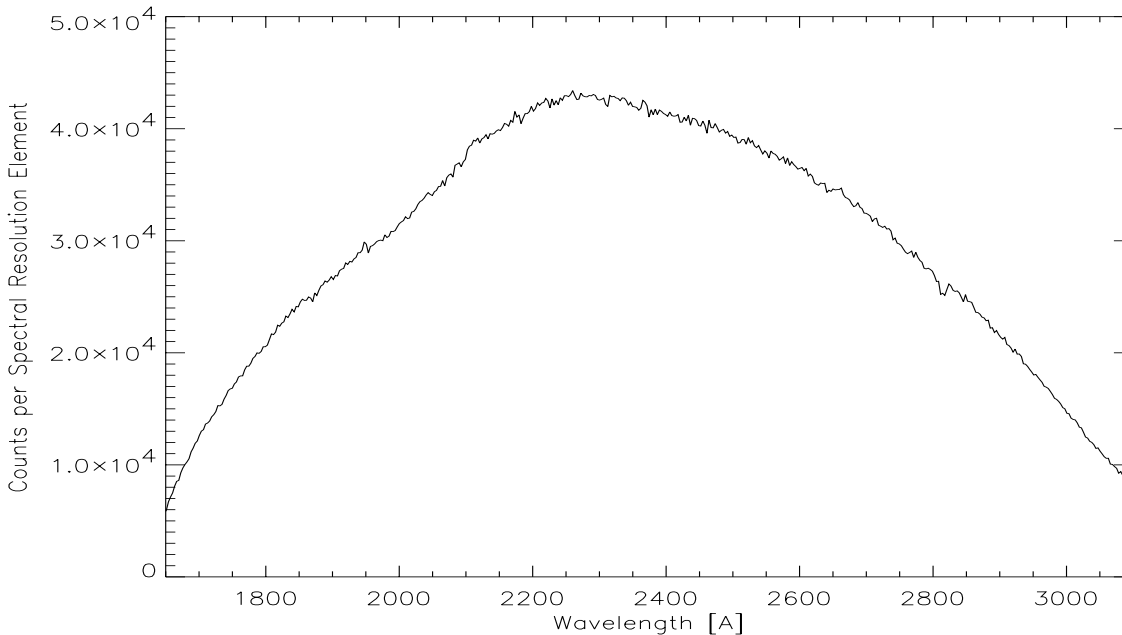


Figure 3: NUV Flat Fielded Single Spectrum of GRW+70D58

To test the S/N limit in the FUV, six G140L spectra of GD+70D58 were coadded. No shifts were applied to align the spectra. Over the region extending from 1347-1502Å the S/N of the composite spectrum is  $\sim 180$ , with S/N  $\sim 300$  from pure counting statistics. It should be cautioned however that these spectra are neither spatially nor spectrally coincident, exhibiting an offset of  $\sim 10$  pixels spectrally and  $\sim 4$  pixels spatially. Consequently a single spectrum of comparable count statistics may yield a slightly lower S/N. These results are also presented in Table 5.

Table 5. FUV Signal-to-Noise Capabilities for a G140L Point Source Spectrum

Star	Spectral Class (B Mag)	Exposure Time	Flat Composition	Spectral Range	S/N (Counting Statistics)	S/N
GD153	DA1 (13.07)	187.1	NO Flat	1280 - 1458	<165>	<85>
				1502 - 1657	<75>	<65>
			G140L	1280 - 1458	<165>	<113>
				1502 - 1657	<75>	<50>
			G140L + G140M	1280 - 1458	<165>	<116>
				1502 - 1657	<75>	<73>
			E140M + E140H	1280 - 1458	<165>	<127>
				1502 - 1657	<75>	<74>
GRW+70D58	DA3 (12.63)	1260.0	NO Flat	1347 - 1502	<295>	<93>
				1502 - 1657	<172>	<81>
			G140L	1347 - 1502	<295>	<184>
				1502 - 1657	<172>	<92>
			G140L + G140M	1347 - 1502	<295>	<189>
				1502 - 1657	<172>	<130>
			E140M + E140H	1347 - 1502	<295>	<168>
				1502 - 1657	<172>	<150>
	G140L + G140M + E140M + E140H	1347 - 1502	<272>	<182>		
		1502 - 1657	<172>	<155>		

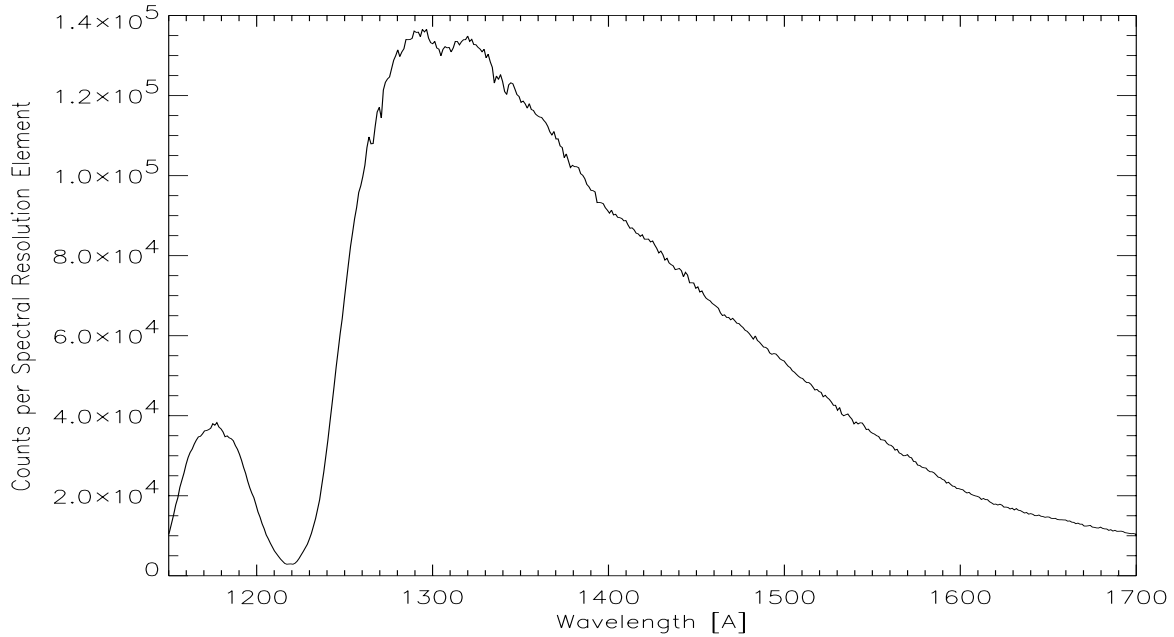


Figure 4: FUV Flat Fielded Combined Spectra of GRW+70D58

Further inspection of the results indicates that at  $S/N \sim 180$  the composition of the flat becomes important. To achieve a  $S/N$  in excess of this, it may be required to use a flat composed solely from the same mode as the observations to eliminate residual angle of incidence effects in the flat. It is also possible that the pre-launch data (E140M and E140H) does not flatten the observations as well as the post launch flats. Note: at the pixels corresponding to longer wavelengths in the G140L observations, the counting statistics in the (G140L + G140M) flat are poorer than the counting statistics in the (E140M + E140H)

flat; this is why the S/N is poorer with the (G140L + G140M) flat over the spectral range from 1502-1657Å.

Even higher S/N ratios are possible if the FP split slit methodology is employed to acquire the observations. Using this technique, exposures are taken through a special set of apertures which offset the spectrum in a purely spectral direction on the detector. Iterative analysis of the data permits solving for both the target spectrum and the flat field response of the instrument. Preliminary analysis of the data (Gilliland et al.) acquired to test this method with STIS indicates that a S/N of >250 per low resolution pixel and >350 per spectral resolution element can be achieved in modes E140M and E140H by employing this technique. The FP split slit results were not presented at the conference because the proposal was executed the same day as the talk.

## 5. Conclusion

STIS is capable of achieving a S/N well in excess of 100:1 in the UV observing modes. In the first order modes, the NUV S/N of  $\sim 150$  is probably limited by count statistics. Limitations of the existing ground-based flat are much less stringent, in principle a S/N exceeding  $\sim 250$  could be achieved with sufficient counting statistics and if the flat has been stable to this limit. In the FUV, we have obtained a S/N  $\sim 190$  by coadding spectra. This method incorporates some additional smoothing, but also does not approach the S/N limit derived from pure counting statistics. Therefore it is the quality of the FUV flat field that is currently limiting the S/N to  $\leq 190$  for the first order FUV modes. Using the FP split slit methodology, the S/N limit is unknown. Preliminary results indicate that the S/N (per low-res pixel) of  $\sim 260$  in the NUV and  $\sim 270$  in the FUV is comparable to the counting statistics.

## References

- Bohlin, R. C., Lindler, D. J., Baum, S. 1996, Instrument Science Report STIS 96-015 (Baltimore:STScI)
- Bohlin, R. C., Lindler, D. J., Kaiser, M. E. 1997, Instrument Science Report STIS 97-07 (Baltimore:STScI)
- Gilliland, R. et al., Instrument Science Report STIS, (Baltimore:STScI), in preparation
- Joseph, C. J. et al. 1995, Proc. SPIE, 1549, 52
- Kimble, R. A., et al. 1998, ApJ, in press
- Timothy, J. G. 1994, Proc. SPIE, 2278, 134
- Woodgate, B. et al. 1998, PASP, submitted